Interconnected assembly factors regulate the biogenesis of mitoribosomal large subunit in trypanosomes

Victor Tobiasson[1†], Ondřej Gahura[2†], Shintaro Aibara[1,3†], Rozbeh Baradaran[1], Alena Zíková[2*], Alexey Amunts[1*]

[1] Science for Life Laboratory, Department of Biochemistry and Biophysics, Stockholm University, 17165 Solna, Sweden.

[2] Institute of Parasitology, Biology Centre, Czech Academy of Sciences, Ceske Budejovice, Czech Republic, Faculty of Science, University of South Bohemia, Ceske Budejovice, Czech Republic.

[3] Current address: Department of Molecular Biology, Max-Planck-Institute for Biophysical Chemistry, Göttingen, Germany.

† The authors contributed equally to this work.

* correspondence to: azikova@paru.cas.cz, amunts@scilifelab.se

Abstract

Mitoribosomes synthesize essential proteins encoded in the mitochondrial genome. They consist of the ribosomal RNA and protein components, coordinated assembly of which is critical for function. Divergent mitoribosomes with reduced RNA and increased protein mass were described in *Trypanosoma brucei*, a mammalian parasite causing African Trypanosomiases. Here, we report that the large subunit of *T. brucei* mitoribosome requires at least 15 biogenesis factors, which we characterized in complex with an assembly intermediate using cryo-EM. These assembly factors form a protein network that spans over 180 Å and connects between functional regions, allowing to coordinate their maturation. The conserved proteins mt-RbgA and mt-EngA are stably bound together at the subunit interface and mitochondrial acyl-carrier proteins play a structural role in constraining the L1 stalk. The characterized assembly intermediate forms an extensive network connecting between functionally important regions of the mitoribosome.

Impact statement

Biogenesis of *Trypanosoma brucei* mitoribosomal large subunit requires a protein network of assembly factors that connects between its functional regions.

Introduction

Mitoribosomes differ from bacterial and cytosolic ribosomes in the ribosomal RNA (rRNA) and protein content, overall size, and structure [1, 2]. In mitochondria of *Trypanosoma brucei*, the mitoribosome consists of over a hundred components, and the ratio of protein to rRNA is unusually high [3, 4]. Since the rRNA forms a compact core of the mitoribosome, and proteins are mostly peripherally associated, an architecture based on the reduced rRNA and supernumerary mitoribosomal proteins suggests a specialized assembly pathway. Indeed, structural characterization of the *T. brucei* mitoribosomal small subunit (mtSSU) provided insights into its assembly pathway that have not been previously known [5]. Compared to the mtSSU, no information is available on the mitoribosomal large subunit (mtLSU) assembly in *T. brucei*.

The mtLSU accommodates the peptidyl transferase center (PTC) that forms peptide bonds between amino acids, tRNA binding sites, the L7/L12 stalk that is responsible for the recruitment of translation factors, the L1 stalk, the central protuberance (CP) that facilitates communication between various functional sites, and exit tunnel for egress of synthesized protein. In bacteria, our understanding of LSU assembly comes from characterization of its final maturation stages [6-8], studies on incomplete LSU particles as a result of protein depletion [9], and *in vitro* reconstitution studies with purified ribosomal RNA and protein components [10]. These studies identified different LSU precursors with assembly factors that play key roles by binding to rRNA components [11]. In mitochondria of *T. brucei*, the mtLSU is lacking many of the rRNA components involved in the canonical pathways. Whether dedicated assembly factors have evolved is not known.

Here, we determine the cryo-EM structure of a native *T. brucei* mtLSU assembly intermediate (pre-mtLSU) with 15 assembly factors. It suggests a biogenesis relying on an extensive protein network formed by assembly factors that connects the maturation of the PTC, L1 and L7/L12 stalks, as well as the CP. Comparison with two bacterial assembly intermediates [12, 13] provides insights into the conserved GTPases EngA and RbgA bound at the subunit interface.

Results and Discussion

Structural determination and composition of the native pre-mtLSU complex

We used a procyclic strain grown in low-glucose medium that maintains translationally active mitochondria. Mitoribosomal complexes were purified directly from *T. brucei* mitochondria. During image processing, in addition to intact monosomes, we detected a pool of free subunits. We focused the analysis on this population and isolated pre-mtLSUs through 3D classification.

896,263 particles were picked using Warp [14], and further processed using RELION [15]. We performed reference-based 3D classification with references generated from a preliminary classification of a screening data set. This resulted in 207,788 particles corresponding to the mtLSU shape but distinct from that of a mature mtLSU of which we found 152,816 particles.

Refinement of angular assignments and subsequent classification using fine-angular searches with a solvent mask identified 32,339 pre-mtLSU particles (Figure 1-figure supplement 1). To improve the angles further, the particles were subjected to masked auto-refinement. Following the CTF refinement, we obtained a reconstruction of a pre-mtLSU that likely reflects a stable premature complex. This is evidenced by the presence of densities corresponding to conserved ribosomal assembly factors.

The cryo-EM reconstruction was refined to 3.50 Å resolution (Figure 1-figure supplement 1). This allowed to build a ~2.2 MDa complex and assign 15 assembly factors, as well as additional mitoribosomal proteins, directly from the density (Figure 1, Figure 1-figure supplement 2). Three distinct features define the overall premature complex: 1) the rRNA domain V is well resolved and the subunit interface consists almost entirely of newly identified assembly factors associated with two conserved GTPases; 2) the L7/L12 stalk proteins are missing, and its rRNA platform is not folded, instead assembly factors occupy similar positions; 3) the CP is absent, and the L1 stalk is shifted inward ~30 Å. Due to these features, compositional and conformational changes are required for the maturation of the pre-mtLSU. In terms of the mitoribosomal proteins, 18 previously identified proteins are missing from the structure of the pre-mtLSU. Seven of these have bacterial homologs (uL10m, uL12m, uL16m, bL27m, bL31m, bL33m and bL36m) and the rest are mitochondria specific (Figure 1, Figure 1-figure supplement 3). Additionally, we assigned sequences to two previously unidentified mtLSU proteins, which we named mL109 and mL110, and observed the presence of mitoribosomal protein uL14m which was not modeled in the mtLSU (Figure 1-figure supplement 2).

Following the previously identified mitoribosomal small subunit assembly factors [5], we adopt a similar nomenclature for the mitochondria specific large subunit factors. Therefore, we reference them as *T. brucei* Large subunit Assembly Factor(s) (TbLAF1-10), while proteins with bacterial homologs are referred to as their bacterial names with the prefix “mt-“.

The identified assembly factors of the mitoribosome include two homologs of bacterial GTPase assembly factors mt-EngA and mt-RbgA, a homolog of the ribosome silencing factor mt-RsfS, a DEAD-box helicase (TbLAF10), two pseudouridinases (TbLAF4 and TbLAF6), a methyltransferase (TbLAF5), two copies of the mitochondrial acyl-carrier protein (mt-ACP), a LYR-motif-containing protein L0R8F8 (TbLAF1), and other lineage-specific proteins with previously unassigned functions (TbLAF2, 3, 7, 8 and 9). In the model, we included only the parts for which clear secondary structure is apparent, and other regions with only partial density visible were modeled as UNK1-13 (Supplementary file 2).

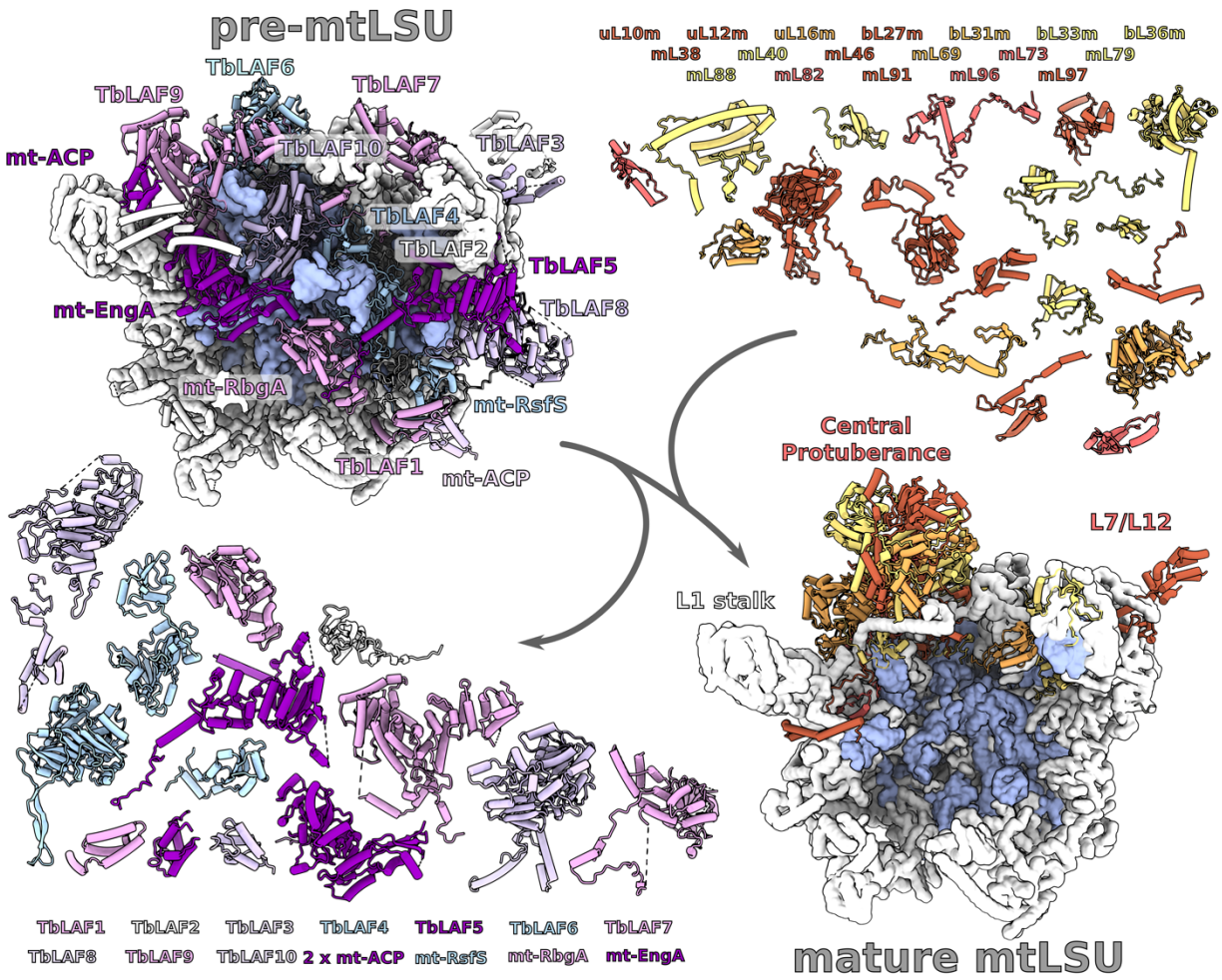

Figure 1. Structure of *T. brucei* pre-mtLSU with 15 assembly factors. Left, the overall modeled structure of the pre-mtLSU (white, rRNA blue) with models of assembly factors (shades of purple) covering the subunit interface, CP, L7/L12 stalk and connecting to the L1 stalk. Right, structure of the mature mtLSU (PDB ID 6HIX) with 18 additional mitoribosomal proteins (shades of orange) absent from pre-mtLSU.

GTPase mt-RbgA is structurally linked to the mitoribosomal core via specific assembly linkers

We started the structural analysis by searching for similar assembly intermediate architectures in bacterial counterparts. Particles with an absent CP were reported previously in RbgA-depleted *Bacillus subtilis* cells. RbgA was then added *in vitro* and shown to bind to the complex, which identified its role as an assembly factor [13]. RbgA is from the Ras GTPase family containing a typically low intrinsic GTPase activity, which is increased in the presence of mature LSU subunits [16]. It has N-terminal GTPase domain and C-terminal helical domain, which forms a five-helix bundle [17]. In the pre-mtLSU structure, we found a conserved mt-RbgA homolog.

Studies in yeasts reported that deletion of mt-RbgA (yeast Mtg1) results in respiration deficiency [18]. In *B. subtilis*, where this assembly factor is essential, the LSU:RbgA complex showed that the N-terminal domain overlaps with rRNA H69 and H71, and the C-terminal helical domain interacts with H62 and H64 [13]. In this position, RbgA displaces the P-site and interacts with the surrounding rRNA, including H92 and H93.Therefore, binding of RbgA requires contacts with rRNA.

In our map of *T. brucei* pre-mtLSU, the corresponding regions forming the rRNA binding site for mt-RbgA are not observed. The nucleotide binding site in mt-RbgA is empty, and fitting a ligand results in clashes with the protein (Figure 2b). However, the comparison of our structure with the *B. subtilis* LSU:RbgA complex (PDB ID 6PPK) shows nearly identical conformation of the factor on the pre-mtLSU complex (Figure 2-figure supplement 1). Even the weak interaction between the mt-RbgA C-terminal domain and the mitoribosomal protein uL14m is conserved (Figure 2).

We found that the conserved position of mt-RbgA in *T. brucei* is maintained through two specialized assembly linkers (Figure 2). The first linker is established between the C-terminal domain and the TbLAF5 N-terminal helix. The latter adopts a crescent shape around the C-terminal domain of mt-RbgA, forming a series of contacts with four out of its five helices (Figure 2). The second linker is provided by TbLAF4 approaching from the mitoribosomal core. It interacts with the mt-RbgA C-terminal domain and contributes a β-strand to a shared β-sheet (Figure 2-figure supplement 2). Together, RbgA is anchored to the flexible core via two dedicated factors that compensate for the lack of rRNA contacts.

TbLAF4 belongs to the family of the site-specific RluD pseudouridine synthases that is involved in the bacterial LSU assembly via formation of pseudouridines at positions 1911, 1915 and 1917 *(E. coli* numbering) in the H69 end-loop [19, 20]. In pre-mtLSU structure, TbLAF4 encircles the immature rRNA nucleotides U1017-U1021 and G1073-U1087 (Figure 3-figure supplement 2), and its active site is occupied by uridine 1017 likley present in H89-93 of the mature rRNA (Figure 2-figure supplement 2B). The N-terminal domain is positioned at the distance of ~80 Å towards the L7/L12 stalk, and this connection plays a key role in coordinating the factors between the different functional sites (Figure 3).

TbLAF5 belongs to the family of SpoU RNA methyltransferases, but appears to have a closed active site that does not allow the binding of its typical S-adenosyl methionine cofactor (Figure 2-figure supplement 2A). It is located peripherally, and bound to the mitoribosome via a C-terminal 24-residue helix interacting with rRNA H41/42, and via TbLAF8 (Figure 2-figure supplement 2). Therefore, TbLAF4 and TbLAF5/TbLAF8 perform a structural scaffolding role for binding mt-RbgA.

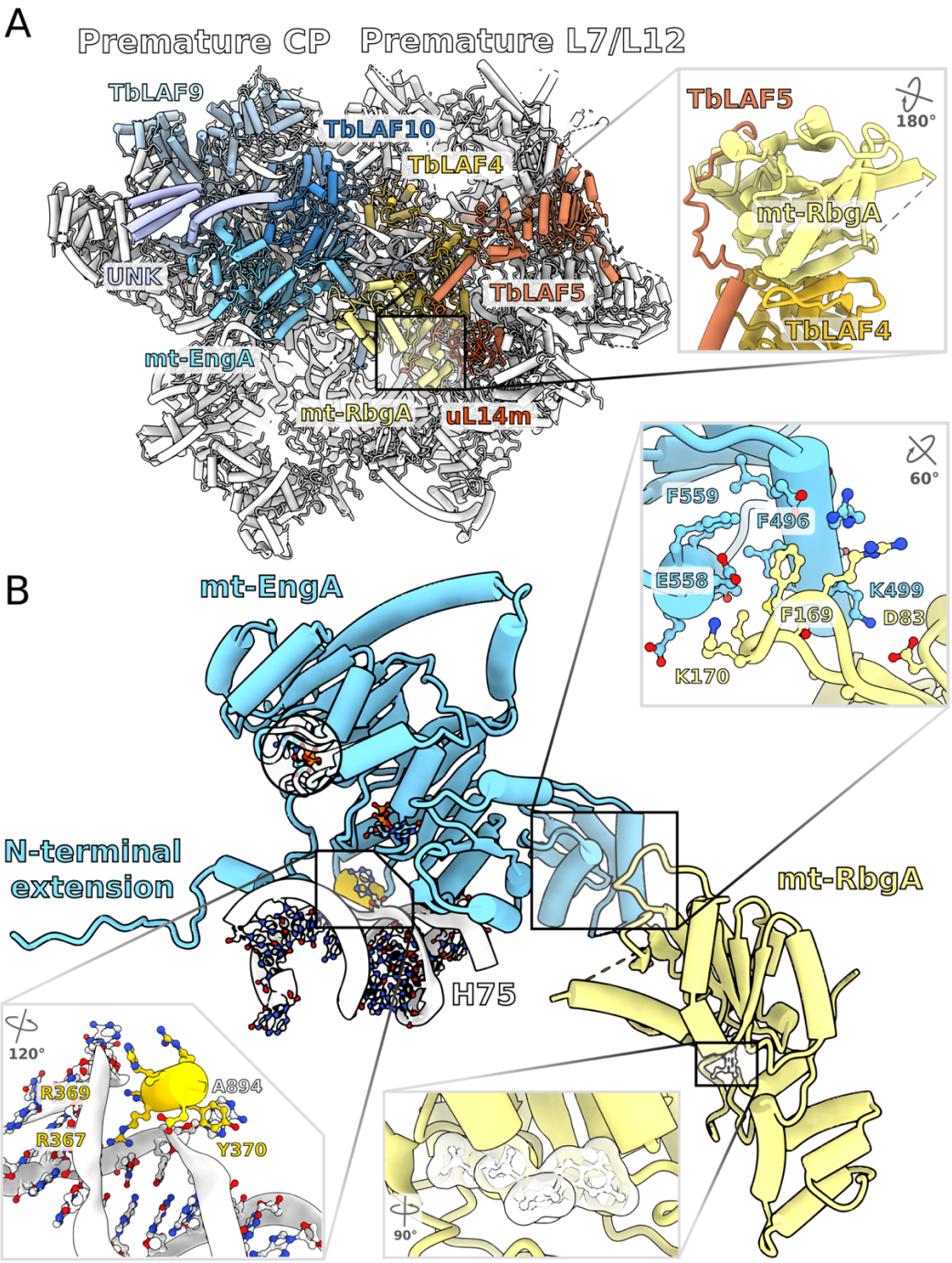

Figure 2. Binding of the mt-RgbA and mt-EngA to the subunit interface. (**A**) mt-RgbA is bound to TbLAF4 and TbLAF5, which are connected to the L7/L12 stalk; mt-EngA is associated with TbLAF9 and TbLAF10, which are connected to the CP. (**B**) A short helix of mt-RgbA (yellow) interacts with a flipped A894 nucleotide from H75 (white). Two GTPs in the GTPase domains on mt-EngA are shown as sticks. The residues forming electrostatic and hydrophobic interactions between mt-EngA and mt-RbgA are shown in the top right inset. Clashes between superimposed GTP in its putative binding site on mt-RgbA are shown in the bottom right inset.

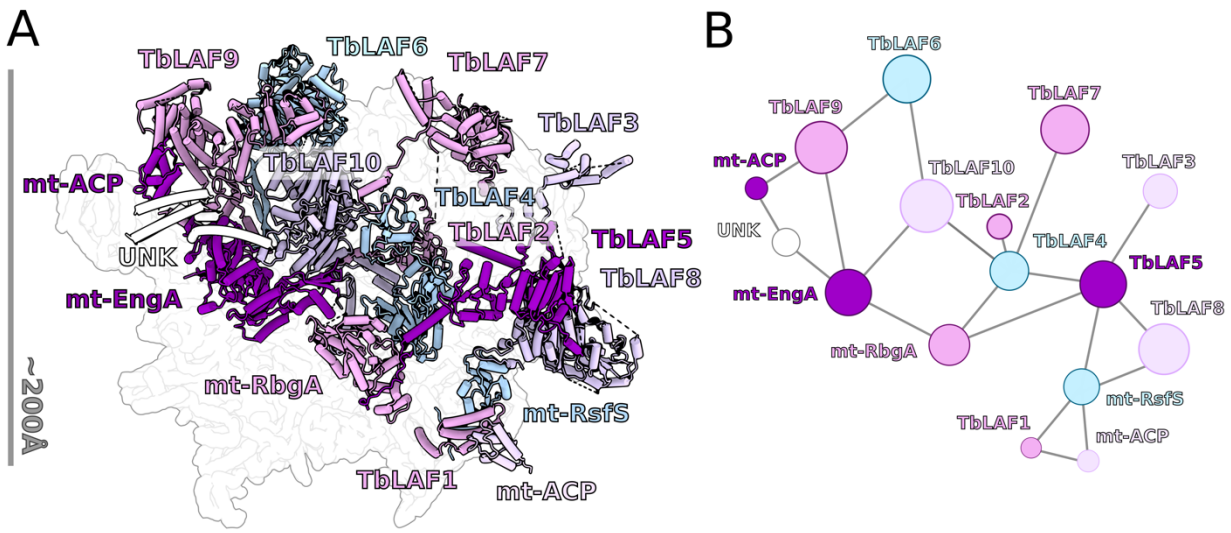

Figure 3. Network of interactions between the assembly factors in pre-mtLSU. (**A**) Assembly factors shown on the background of the pre-mtLSU density map, featuring the interconnection. (**B**) Schematic of protein-protein network. The node size represents the relative molecular mass of the protein. All the assembly factors are interconnected with each other.

GTPase mt-EngA is stabilized via protein extension

In the subunit interface, we identified another stably bound conserved GTPase homolog, mt-EngA. It contains two tandemly arranged GTPase domains and a C-terminal K homology (KH) domain, which is pointed towards the PTC. We could model two GTPs in the GTPase domains (Figure 2B). The positioning is identical to bacteria, suggesting a functional conservation. The assembly factor occupies the space between the PTC and the E-site (Figure 2-figure supplement 1), and a role in chaperoning rRNA has been proposed [12]. The comparison with *E. coli* LSU:EngA complex reveals conformational differences that further highlight the unconventional nature of the *T. brucei* protein-rich system, and its role in the stabilization of the conserved assembly factors.

Firstly, the N-terminal GTPase domain is extended by 60 residues, with residues 101-108 stabilizing a helix-turn-helix motif (275-305), which remained unresolved in the bacterial complex (Figure 2-figure supplement 1B). This motif is important for the stabilization of EngA, because one helix is stacked against a helix of TbLAF10, whereas the other forms a helical bundle with an unidentified protein (Figure 2-figure supplement 3). TbLAF10 is one of the largest mitoribosomal assembly factors, which spans 110 Å through the rRNA core to the CP (Figure 2 and 3, Figure 3-figure supplement 1). It has the contact area with rRNA of ~8400 Å and keeps the nucleotides U904-A917 as well as U953-A965 (putative H80-83) in a premature conformation (Figure 3).

Secondly, the N-terminal residues 72-75 stabilize a short helix (residues 367-374), which is buried within rRNA groove via Arg367 and Arg369 (Figure 2b). It disrupts the local structure of

194 H75 and stabilizes the flipped nucleotide A894 (Figure 2b). This loop is also highly charged in
195 the corresponding *E.coli* structure, but does not adopt the helical conformation. Finally, the N-
196 terminus forms additional contacts with five mitoribosomal proteins (bL28m, bL35m, bL19m,
197 mL64, mL74), a stabilizing protein mass that compensates for the missing rRNA in this region.
198 Overall, while the N-terminal GTPase domain aligns well with the bacterial EngA, its interacting
199 partners in our structure are proteinaceous and specific to *T. brucei*.

200 The conserved globular domains of mt-EngA are associated with the pre-mtLSU core via
201 TbLAF9. Its three helices from the N-terminus encloses the N-terminal GTPase domain helix
202 230-242 (Figure 2- figure supplement 3). Here, TbLAF9 replaces the missing rRNA H82, H88
203 and protein L1, which binds the EngA N-terminal GTPase domain in bacteria. TbLAF9 spans
204 over 100 Å to the top of the CP, where it also stabilizes unwound rRNA (Figure 1-figure
205 supplement 3, Figure 3-figure supplement 1). Thus, mt-EngA is stably bound via protein
206 extension and also associated with the protein-based scaffold of assembly factors, including the
207 high molecular weight TbLAF9 and TbLAF10, which are connected to the CP (Figure 3).

208

209 **The module mt-RbgA:mt-EngA coordinates maturation of interfacial rRNA**

210 The process of the LSU assembly is dynamic with cooperative action of different assembly
211 factors [9, 11]. Although RbgA and EngA have previously been visualized separately on the
212 bacterial LSU though deletion and reconstitution experiments, our cryo-EM structure shows both
213 factors simultaneously associated with the mt-LSU and with each other. This is attributed to the
214 stabilization by the protein linkers and extensions at the subunit interface. The presence of both
215 factors rationalizes why rRNA domain V is unexpectedly well resolved compared to the mature
216 mtLSU [4]. We were able to model 33% more nucleotides relative to the mature LSU (Figure 4),
217 thereby showing that the H89-93 region does not occupy the expected final position and
218 highlighting a need for prominent remodeling during maturation (Figure 4, Figure 4- figure
219 supplement 1).

220 The contacts between mt-RbgA and mt-EngA are formed between the N-terminal domain and
221 KH domains, respectively (Figure 2b). The shared surface area is ~540 Å, and each of the
222 domains is also associated with conserved rRNA. The formed contacts between mt-RbgA and
223 mt-EngA include electrostatic interactions, as well as hydrophobic residues (Figure 2b). Since
224 the structures and positions of both factors are conserved, these results indicate that a similar
225 overall mode of interaction could take place in other translational systems.

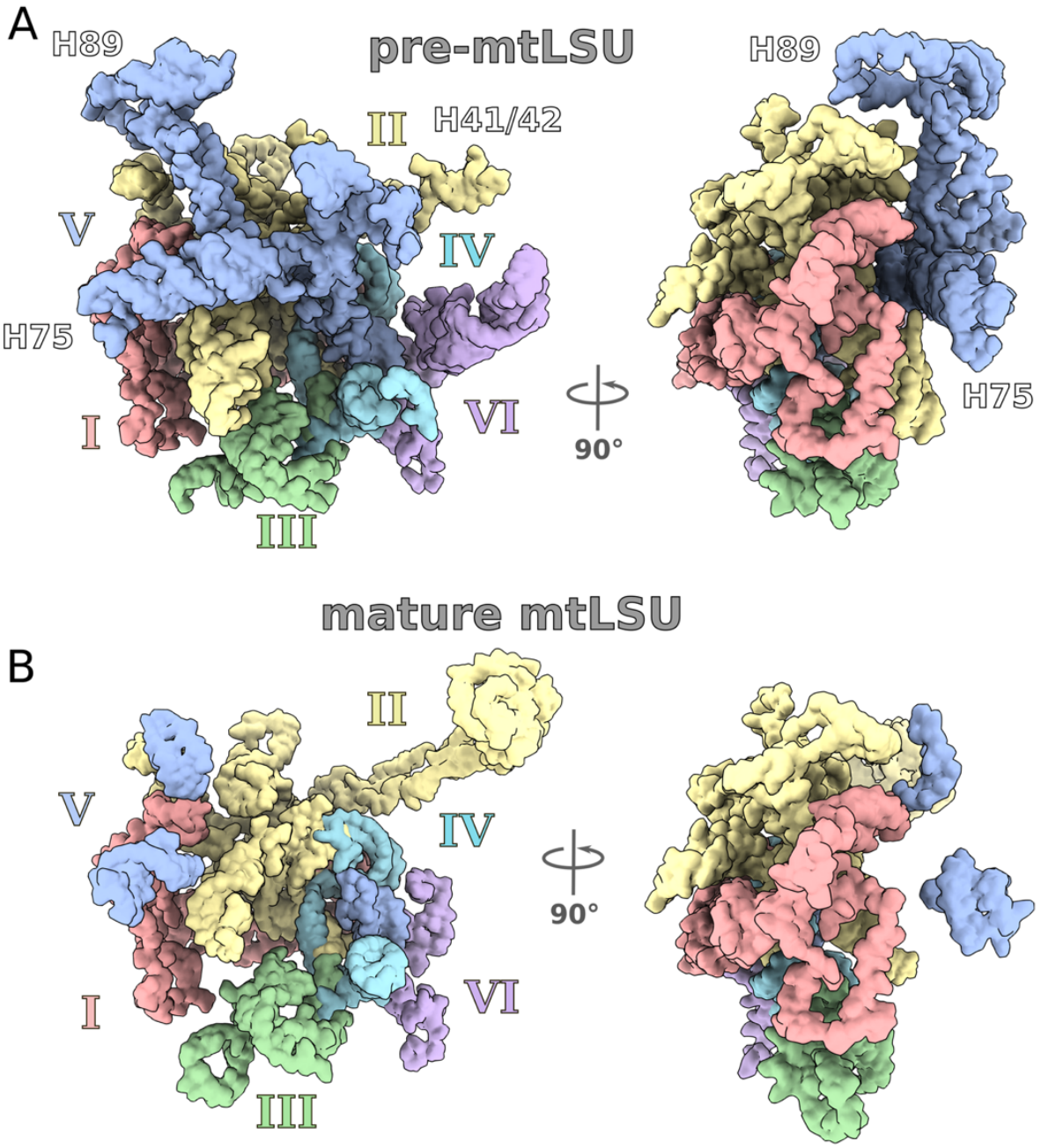

Figure 4. Tertiary structure of rRNA in pre-mtLSU (A) and mature mtLSU (B). Shown from the subunit interface (left) and sideview (right). (A) Two views of rRNA related by 90° are shown with each domain in a different color. Domain V is more structured in pre-mtLSU, and H89-93 adopt a different conformation. Domain II that is responsible for L7/L12 stalk is largely disordered.

235 **Progressive maturation of the L7/L12 stalk**

236 The L7/L12 stalk is a universal mobile element that associates translational protein factors with
237 the A-site. It typically consists of the rRNA platform that connects to the flexible factor-
238 recruiting series of bL12m copies. The ubiquitous ribosomal proteins uL10m, uL11m and
239 mitochondria-specific mL43 link the different components together. In our structure, most of the
240 protein constituents of the stalk are missing and others adopted conformational changes (Figure
241 5).

242 In the region of the platform, at least three proteins (uL16m, bL36m, mL88) associated with the
243 rRNA in the mature mtLSU are absent. Consistently, the rRNA platform is not folded, as the
244 folding relies on the missing mitoribosomal proteins. Instead, the N-terminal domain of TbLAF4
245 extends from the subunit interface to occupy part of the space left by uL16m absence (Figure 5A
246 and B). It binds two specific assembly TbLAF2 and TbLAF7 (Figure 5A). TbLAF2 mediates
247 further contacts with the core of the pre-mtLSU. TbLAF7 consists of 7-stranded beta-barrel, 12
248 α-helices, and 63-residue tail inserted into the mitoribosomal core. The structure suggests that
249 both TbLAF2 and TbLAF7 need to dissociate for the missing mitoribosomal proteins to
250 assemble (Figure 5A).

251 In the factor-recruiting region, instead of the terminal bL12m copies, TbLAF3 and density
252 corresponding to UNK6 form a protrusion (Figure 5A). They comprise a protein continuum of at
253 least 13 helices associated with each other, and attached to the platform region through 30-
254 residue C-terminal tail of TbLAF3, forming a helical bundle with mL75 (Figure 5A and C).
255 Overall, this protein module extends ~70 Å from the core in a similar fashion to the L7/L12
256 stalk, and both appear to be mutually exclusive.

257 The position of the uL10m N-terminus, which links the stalk to the body, is occupied by
258 TbLAF3 C-terminus. It interacts with mL43, resulting in its helix being bent by 90° (Figure 5B).
259 This conformational change and the lack of uL10m is correlated with ~15 Å shift of uL11m to
260 occupy the formed void (Figure 5B). Nevertheless, TbLAF3 is only peripherally associated with
261 mL43, and therefore in principle the protrusion can be replaced by the mature L7/L12 stalk
262 independently.

263 Together, our structure proposes a working model for the L7/L12 stalk maturation through four
264 steps: 1) TbLAF4, which is extended from the subunit interface anchoring mt-RgbA, has to be
265 removed. 2) TbLAF2:TbLAF7 is evicted from the ribosomal core; 3) rRNA platform is folded;
266 4) uL16m, bL36m, and mL88 are recruited to the rRNA platform; 5) TbLAF3 is removed, and
267 uL11m, mL43 adopt their mature conformations; 6) bL10m and bL12m stalk proteins are
268 associated.

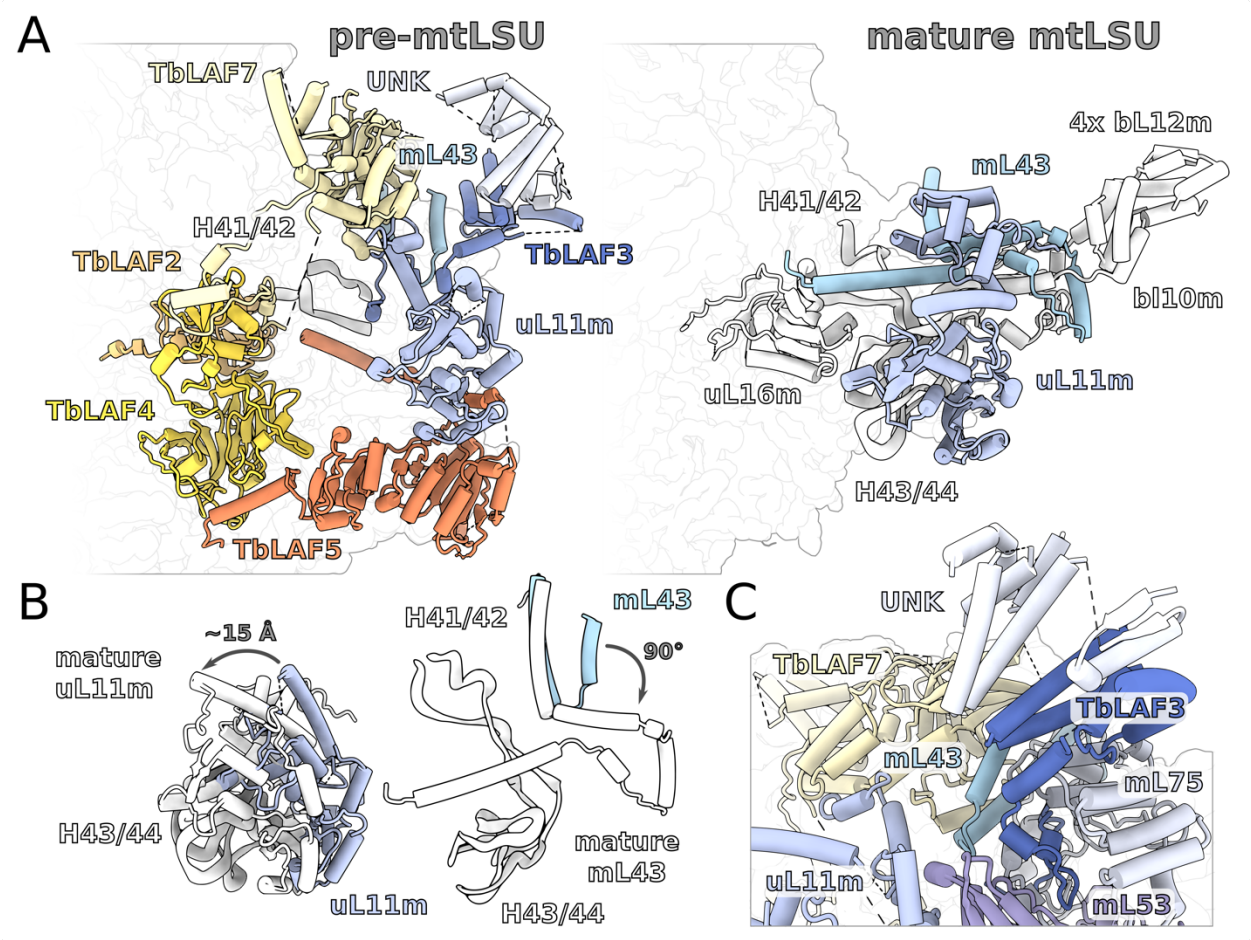

Figure 5. Assembly of the L7/L12 stalk. (**A**) In pre-mtLSU, TbLAF4 extends from the subunit interface to occupy the position of uL16m in the mature mtLSU. TbLAF2 and TbLAF7 are bound at the stalk base to the unfolded rRNA H41/42. TbLAF3 and additional protein form a protrusion similar to bL10m:bL12m. Other mitoribosomal protein removed for clarity. (**B**) Conformational changes from pre-mtLSU (green) to mature mtLSU (white) include mL43 and uL11m. **(C)** TbLAF3, mL75, and UNK protein form continuum of at least 13 helices that is peripherally associated.

Below the L7/L12 stalk we identified three additional proteins: an ortholog of the bacterial ribosome silencing factor mt-Rsf, a LYR (leucine-tyrosine-arginine) motif containing protein L0R8F8 (TbLAF1), as well as an associated mt-ACP (Figure 1 and 3). The human and fungi mitochondrial counterparts of these three proteins have been shown to be involved in late assembly stages of the mitoribosome [21,22]. In our structure, the module is further stabilized by mL85, however unlike in human and fungi, it does not appear to obstruct the binding of the mature mtSSU, likely because of the reduced rRNA and different overall shape. This suggests that in order for this protein module to act according to the same mechanism as found in the

286 mitoribosomes from other species, a complementary structural domain from pre-mtSSU would
287 be required for steric hindrance.
288

289 **Assembly of the CP is linked to the subunit interface and L1 maturation via mt-ACP**

290 The most prominent architectural feature of the pre-mtLSU complex is the absence of the CP,
291 which is a universal ribosomal element that defines the shape of the LSU and forms bridges with
292 the SSU head. In mitoribosomes, the CP is particularly protein-rich [23-28]. The acquisition of
293 those mitochondria-specific proteins took place in the early evolution of the mitoribosome [29].

294 In the *T. brucei* pre-mtLSU, all the CP mitoribosomal proteins are missing and the high
295 molecular weight assembly factors TbLAF6 (69 kDa) and TbLAF9 (67 kDa) are present (Figure
296 1 and Figure 6A). TbLAF6 binds on the solvent side of the CP covering the otherwise exposed
297 rRNA, which only engages in limited base pairing. This assembly factor is annotated as a
298 putative TruD family pseudouridine synthase. However, in our structure, it displays a two-strand
299 antiparallel β-sheet near the catalytic site protruding into the ribosomal core interacting with four
300 mitoribosomal proteins (uL15m, bL28m, bL35m, mL74) (Figure 6B). TbLAF9 is an exclusively
301 helical protein, comprised of at least 29 helices. It binds on top of the rRNA, providing an
302 additional protective protein cap (Figure 6A).
303 Two of the TbLAF9 helices interface with a four-helix bundle, which we identified as mt-ACP
304 (mt-ACP2) in the density with a local resolution of 3.5 Å (Figure 1-supplement figure 2). Since
305 mt-ACP proteins are known to form interactions with Leu-Tyr-Arg (LYR)-motif proteins, we
306 compared the mt-ACP1-TbLAF1 module from the subunit interface with the CP mt-ACP2
307 region (Figure 6C). The helices of the LYR-motif protein TbLAF1 align well with an unassigned
308 density corresponding to three helices associated with the mt-ACP2. The interactions in both
309 cases are mediated by the 4′-phosphopantetheine (4′-PP) modification of mt-ACP, resembling
310 the canonical interactions between mt-ACP and the LYR-motif proteins. The 4′-PP appears to be
311 acylated as indicated by the density (Figure 6C).
312 The importance of the mt-ACP2 protein module in our structure is of twofold. First, it directly
313 binds the L1 stalk and locks it in an inward facing nonfunctional conformation (Figure 1).
314 Second, it is involved in mt-EngA stabilization by forming a U-shaped continuum from TbLAF9
315 on the solvent side of the CP to the subunit interface (Figure 3). It therefore contributes to the
316 protein network connecting between the various functional sites. Thus, mt-ACP2 is a principal
317 partner in the mitoribosomal assembly pathway. In the pre-mtSSU, mt-ACP was also identified
318 as one of the assembly factors [5]. In addition, ACPs in mitochondria act as subunits of the
319 electron transport chain [29] and Fe-S cluster assembly complexes [30]. This further supports the
320 proposed concept that mt-ACPs could act as signaling molecules in an intramitochondrial
321 metabolic state sensing circuit [31].
322

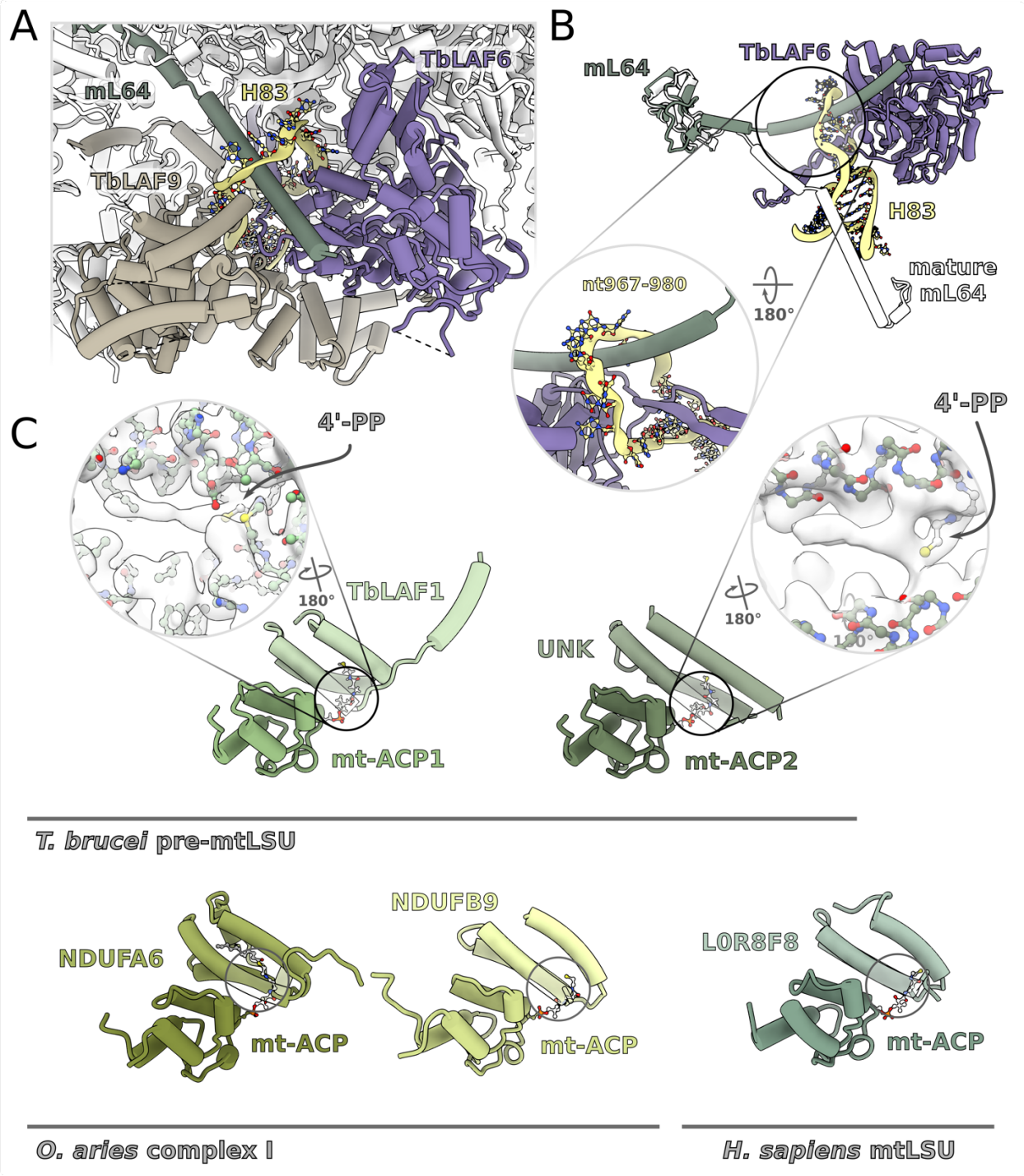

Figure 6. The CP assembly intermediate. (**A**) TbLAF6 and TbLAF9 form the CP in the pre-mtLSU. (**B**) TbLAF6 and mL64 elements are inserted through rRNA loop corresponding to H83. Conformational change of mL64 from pre-mtLSU to mature mtLSU (white) is indicated. (**C**) Comparison between the mt-ACP1:TbLAF1 (left) and the CP mt-ACP2 region (right). The density (white) for acylated 4′-PP is indicated. Bottom panel, comparison with mt-ACP and associated LYR-motif proteins from complex I (PDB ID 5LNK) and human mitoribosome (PDB ID 5OOM) shows the canonical interactions.

At the CP, the assembly factors cooperatively bind unwound rRNA nucleotides U934-U953 (H83) (Figure 6A). Remarkably, the rRNA forms a loop 25 Å in diameter that contains the TbLAF6 β-sheet and mL64 C-terminal helix, both inserted from the opposite directions (Figure B). The conserved helix of mL64 is shifted in our pre-mtLSU structure ~30 Å from the final location on the mature LSU, where it aligns the E-site (Figure 6B). Interestingly, this is also one of the most conserved mitoribosomal proteins across species [32], and its role in tRNA translocation has been established [33]. To switch to the conserved and mature position, the extended C-tail of mL64 has to liberate from the rRNA loop and then undergo a large conformational shift towards the L1 stalk. Subsequently, the C-tail is inserted to its mature position, where it contacts CP components absent from the assembly intermediate. Since the L1 stalk is shifted, the maturation towards a mature LSU is likely to occur in a concerted manner.

Conclusions

Together, our structure of the *T. brucei* pre-mtLSU in complex with at least 15 assembly factors reveals that mt-RbgA and mt-EngA are held by protein linkers and interact with each other. The analysis of the different sections shows that high molecular weight TbLAF4, TbLAF9 and TbLAF10 proteins form a network that spans over 180 Å and connects the subunit interface with the progressive maturation of the L7/L12 stalk, L1 stalk, and the assembly of the CP. This design would allow biogenesis steps towards the mature mtLSU to be coordinated. In this regard, the tight binding of the mt-ACP2 with partner proteins at the CP emphasizes its structural role in forming the connections. For the L7/L12 stalk, the structure further suggests a sequential mechanism of assembly, and protein replacement that can be a final control. Overall, the protein-based communication allows the formation of the here reported stable assembly intermediate that is ready to progress through the biogenesis pathway.

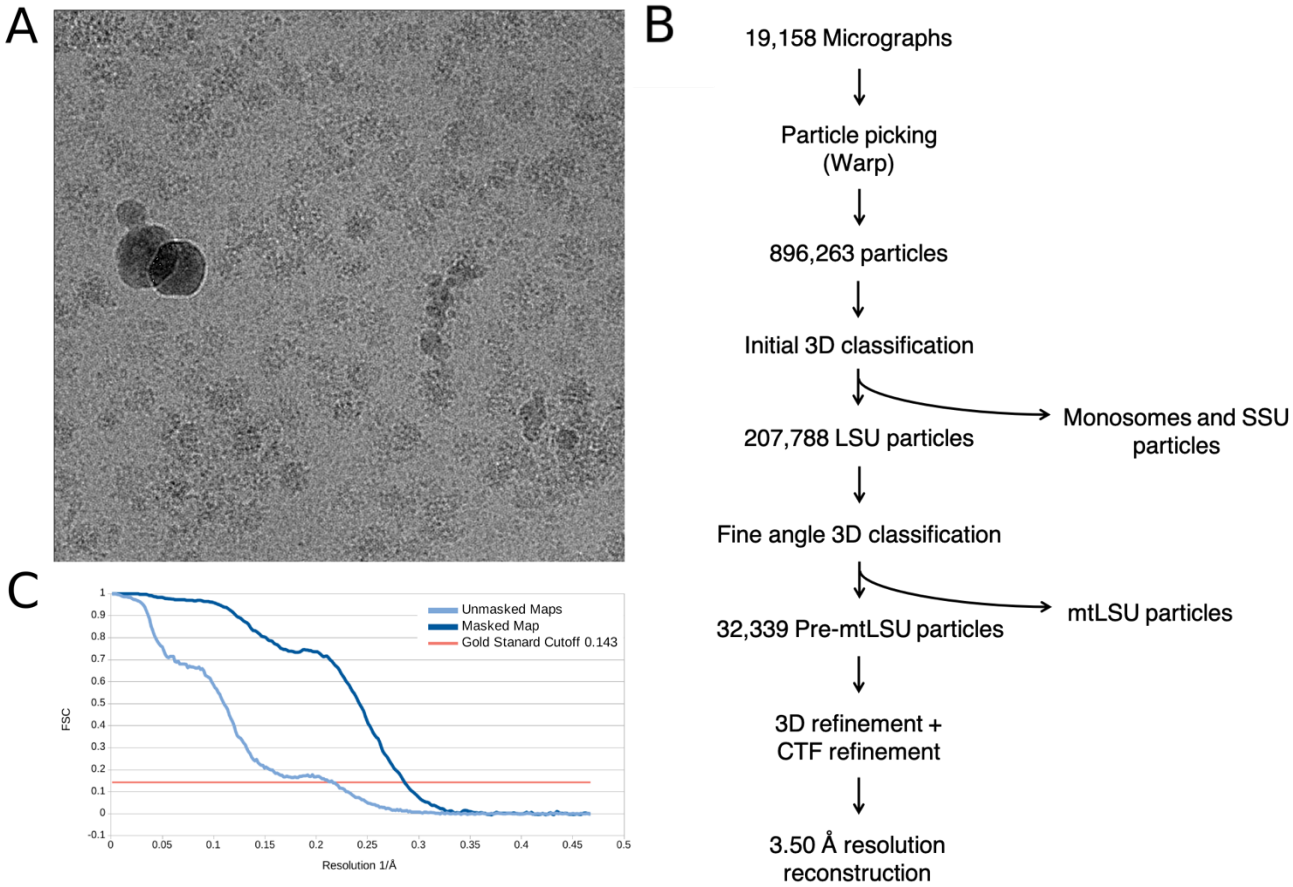

Figure 1-figure supplement 1. Cryo-EM data processing. (**A**) Representative micrograph. (**B**) Processing workflow. (**C**) Fourier shell correlation (FSC) curves. Resolution is estimated based on the 0.143 FSC cut-off criterion (red line).

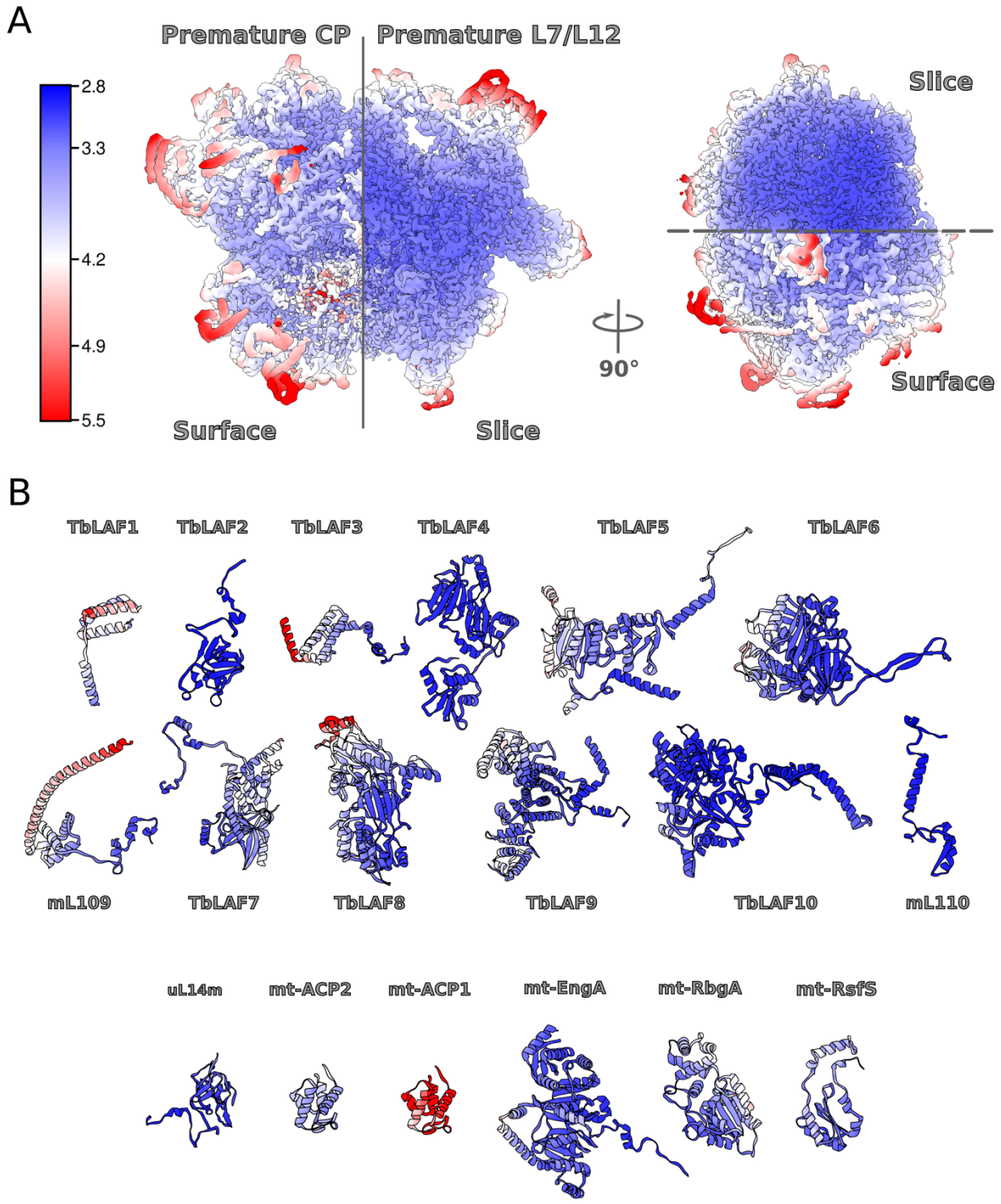

Figure 1-figure supplement 2. (**A**) final map colored by local resolution. (**B**) Models for individual assembly factors and newly identified proteins colored by local resolution of the density in the corresponding regions.

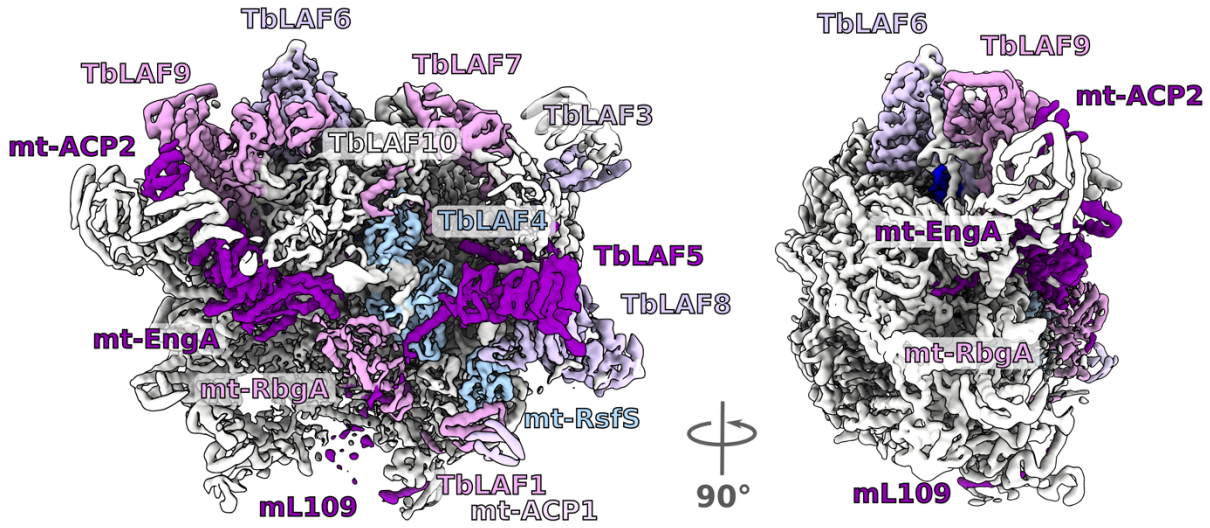

Figure 1-figure supplement 3. Comparison of the cryo-EM maps between pre-mtLSU and mature mtLSU in two 90°-related views. Assembly factors (shades of purple) are indicated.

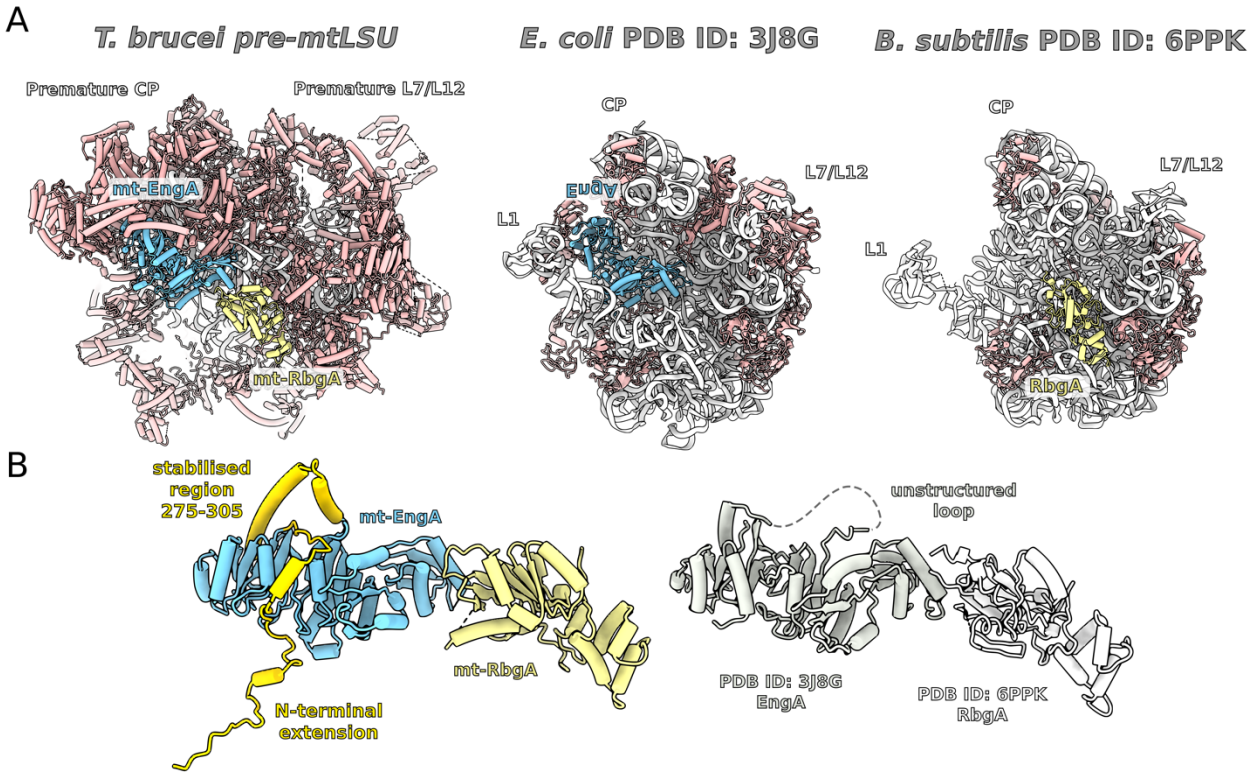

Figure 2-figure supplement 1. The binding of mt-RbgA and mt-EngA at the mtLSU interface. (**A**) Comparison between pre-mtLSU and bacterial counterparts *E. coli* 50S:EngA (PDB ID 3J8G) and *B. subtilis* 45S:RbgA (PDB ID 6PPK) shows nearly identical positions of the factors on their ribosomal complexes. (**B**) Comparison between mt-RbgA:mt-EngA module from the pre-mtLSU and superimposed bacterial counterparts combined from the two structures from (A) shows nearly identical conformations of the factors. The N-terminal extension of mt-EngA (orange) is buried in the mitoribosomal core and stabilizes the binding, as well as 275-305 region (orange). The comparison suggests that a similar mode of interaction would exist in bacterial ribosomal assembly intermediates, where both factors present.

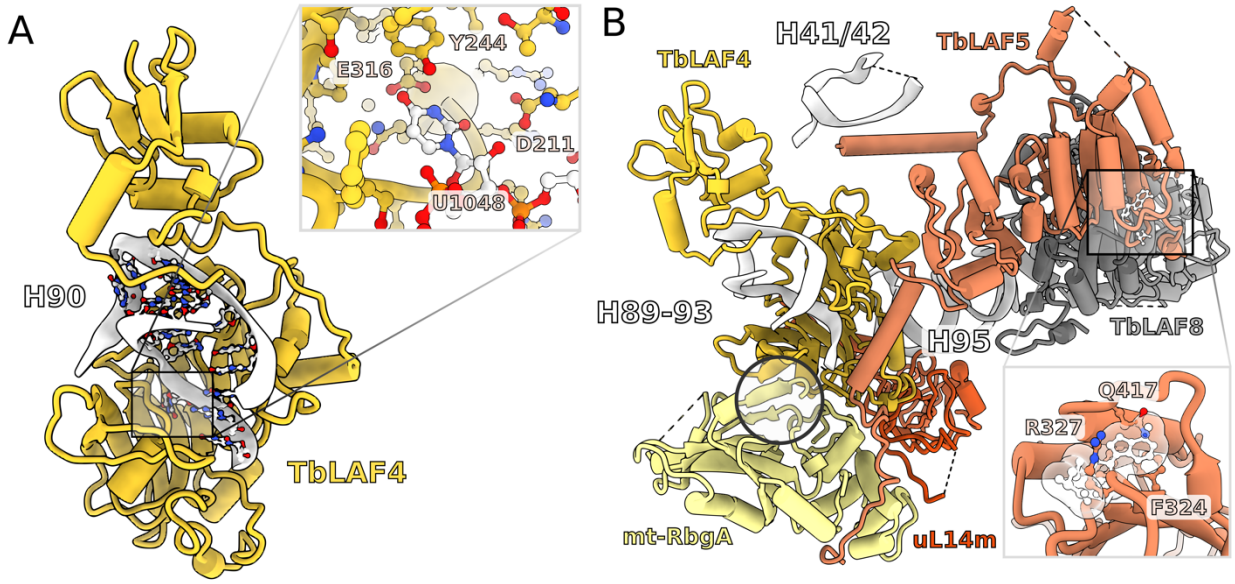

Figure 2-figure supplement 2. (**A**) The active site of TbLAF4 (yellow) is occupied by uridine 1048. (**B**) The factor TbLAF4 (yellow) binds mt-RbgA (pale-yellow) via a shared β-sheet (circled). The methyltransferase site of TbLAF5 does not allow for the binding of S-adenosyl methionine cofactor (white sticks and surface) due to clashes with the protein residues (red).

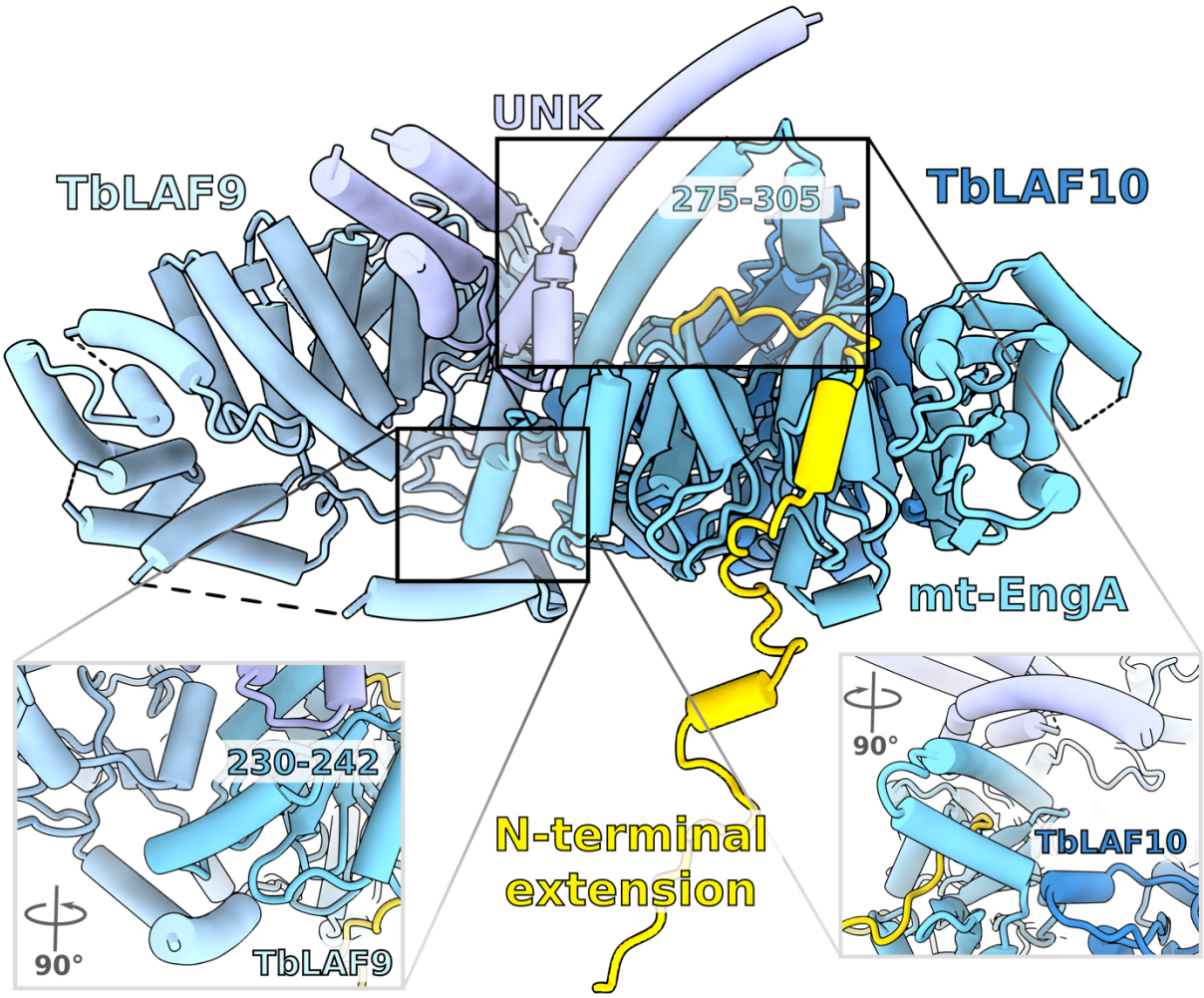

Figure 2-figure supplement 3. N-terminal extension (yellow) of mt-EngA stabilizes helix-turn-helix (275-305), which forms interaction with TbLAF10 on the other side (bottom right panel), and a helical bundle with an unidentified protein UNK that is in contact with TbLAF9.

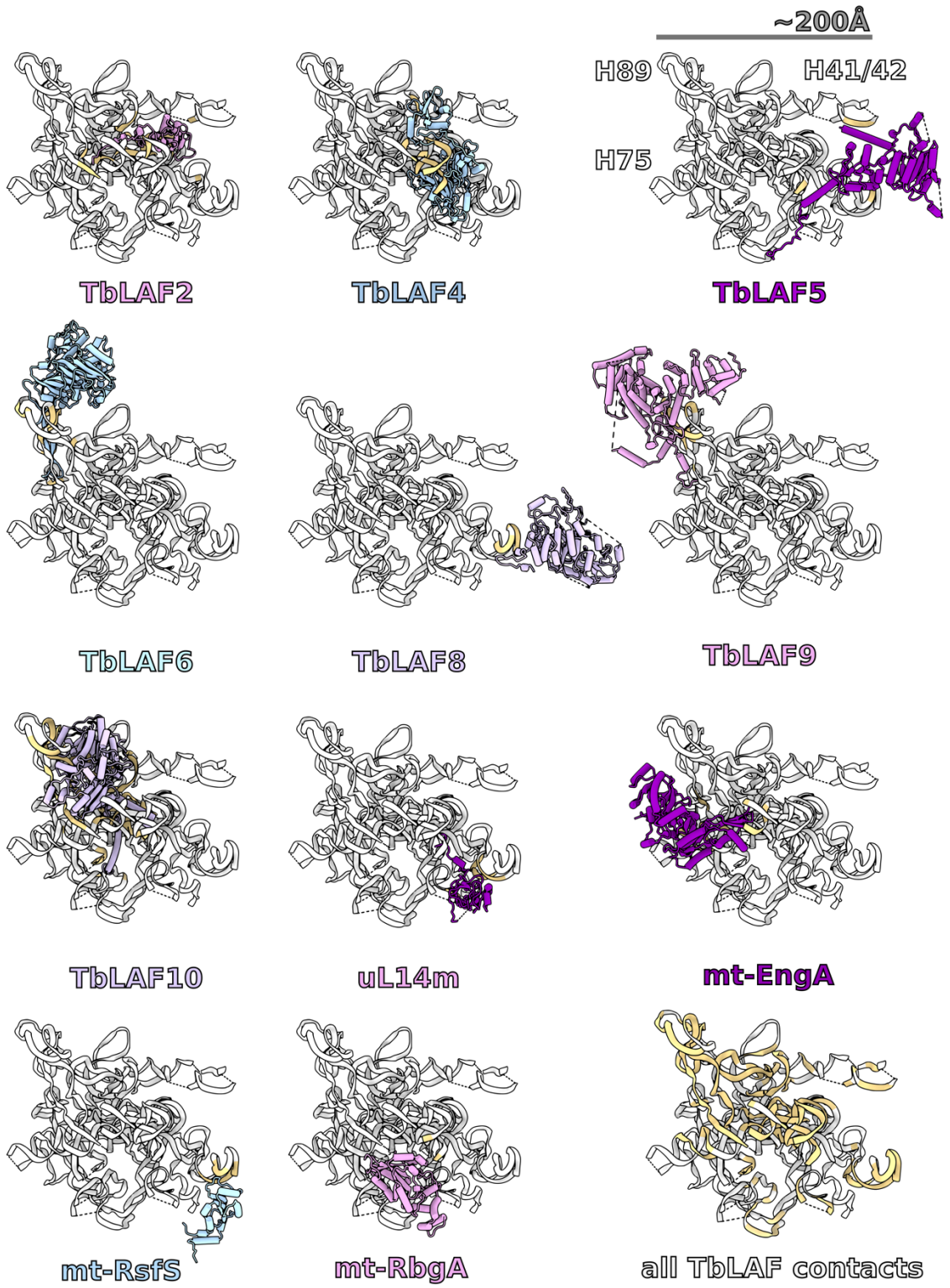

Figure 3-figure supplement 1. Binding of assembly factors to rRNA. For each panel rRNA is shown with an individual protein characterized in the structure for the first time. Bottom right panel illustrates the total RNA that is involved in the interactions (yellow) with the assembly factors.

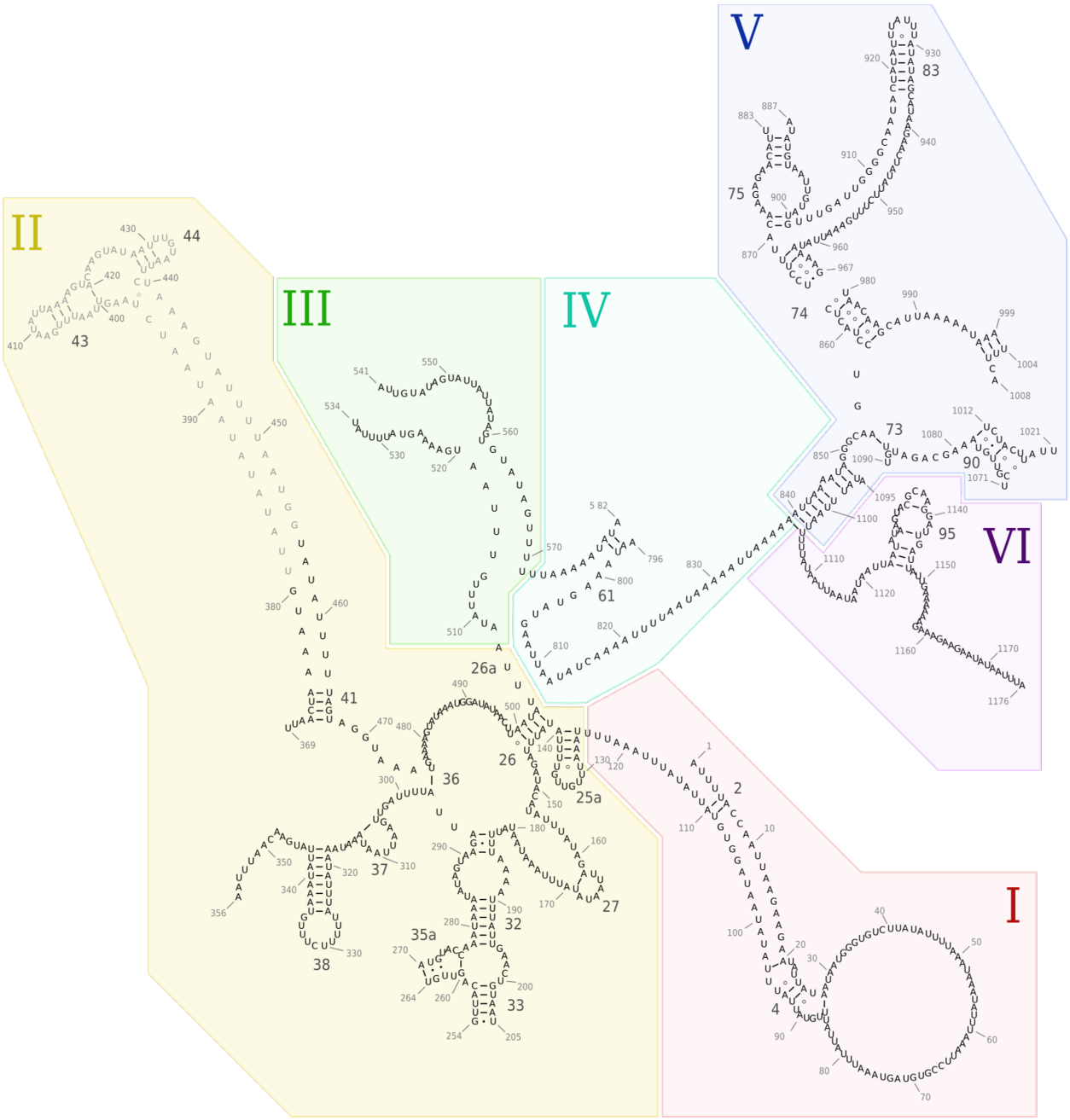

Figure 4-figure supplement 1. Secondary structure rRNA diagram derived from the model and colored by domain. Unbuilt sections that appear in the mature mtLSU are shown in gray. Domains in Roman numerals.

425 **Supplementary File 1. Cryo-EM data collection, refinement and validation statistics**
426

	Consensus map
Data collection and processing	
Magnification	130000x
Voltage (kV)	300
Electron exposure (e–/Å^2)	35
Defocus range (μm)	-0.8 ~ -3.5
Pixel size (Å)	1.05
Symmetry imposed	C1
Initial particle images (no.)	896,263
Final particle images (no.)	32,339
Map resolution (Å) FSC threshold 0.143	3.50
Map resolution range (Å)	3.0~10
Refinement	
Map sharpening *B* factor (Å^2)	-70
Model composition	
Non-hydrogen atoms	146831
Protein residues	17415
Ligands	10
B factors min/max/avg (Å^2) Protein Nucleotide Ligand	 17/172/68 22/281/57 35/194/61
R.m.s. deviations Bond lengths (Å) Bond angles (°)	 0.002 0.46
Validation	
MolProbity score	1.65
Clashscore	6.7
Poor rotamers (%)	0.35
Ramachandran plot	
Favored (%)	95.6
Allowed (%)	4.10
Disallowed (%)	0.03

427
428

429 **Supplementary File 2. Summary of pre-mtLSU components**

Alias	Chain ID	TriTrypDB Gene ID (Lister strain 427)	TriTrypDB Gene ID (reference strain TREU927)	Uniprot ID (reference strain TREU927)	Full size	Modeled residues	Comment
12S rRNA	AA	N/A	N/A	N/A	1176	1-205, 254-264, 270-356, 369-380, 404-413, 445-450, 456-534, 541-582, 591-594, 796-883, 887-967, 980-999, 1004-1008, 1012-1021, 1071-1090, 1095-1176	
uL3m	AE	Tb427.03.5610	Tb927.3.5610	Q580R4	473	38-265, 272-404	
uL4m	AF	Tb427tmp.02.3810	Tb927.11.6000	Q385G8	351	18-459	
bL9m	AI	Tb427.05.3410	Tb927.5.3410	Q57UC5	263	9-220	
uL11m	AK	Tb427.02.4740	Tb927.2.4740	N/A	342	26-200, 207-235, 239-306	239-306 built as UNK
uL13m	AN	Tb427.04.1070	Tb927.4.1070	Q580D5	202	10-180	
uL14m	XG	Tb427.04.930	Tb927.4.930	Q580C1	217	20-107, 114-189	
uL15m	AP	Tb427.05.3980	Tb927.5.3980	Q57U68	374	10-136, 150-322, 354-363	
bL17m	AR	Tb427.08.5860	Tb927.8.5860	Q57YI7	301	11-266	
bL19m	AT	Tb427.01.1210	Tb927.1.1210	Q4GZ98	144	2-139	
bL20m	AU	Tb427tmp.01.1930	Tb927.11.10170	Q383R2	213	10-140, 162-205	
bL21m	AV	Tb427.07.4140	Tb927.7.4140	Q57UP4	188	6-185	
uL22m	AW	Tb427.07.2760	Tb927.7.2760	Q57Y86	278	2-278	
uL23m	AX	Tb427tmp.03.0260	Tb927.11.870	Q387G3	246	64-228	
uL24m	AY	Tb427.03.1710	Tb927.3.1710	Q57ZE0	378	1-311, 318-340	
bL28m	A1	Tb427.06.4040	Tb927.6.4040	Q586A2	241	10-226	
uL29m	A2	Tb427tmp.160.5240	Tb927.9.7170	Q38EM7	471	9-233, 248-471	
uL30m	A3	Tb427tmp.211.0230	Tb927.9.8290	Q38ED8	218	51-200	
bL32m	A5	Tb427.04.2330	Tb927.4.2330	Q584F4	80	26-80	2Fe-2S cluster binding

bL35m	A8	Tb427.10.1870	Tb927.10.1870	Q38C55	181	40-181	
mL41	Ae	Tb427tmp.01.1600	Tb927.11.9830	Q383U6	197	47-161	
mL42	Af	Tb427tmp.01.1840	Tb927.11.10080	Q383S1	189	41-173	
mL43	Ag	Tb427.04.4600	Tb927.4.4600	Q583E5	260	2-186	
mL49	Al	Tb427.05.3110	Tb927.5.3110	Q57Z82	218	37-101, 114-218	
mL52	Ao	Tb427tmp.02.2250	Tb927.11.4650	Q385V2	152	19-151	
mL53	Ap	Tb427.07.2990	Tb927.7.2990	N/A	309	16-303	
mL63	At	Tb427.07.7010	Tb927.7.7010	Q57XS1	154	10-154	
mL64	Av	Tb427tmp.01.3500	Tb927.11.11630	Q383B7	242	27-222	NAD binding
mL67	BA	Tb427tmp.55.0016	Tb927.11.1630	Q386Z1	831	27-83, 130-328, 335-542, 562-824	
mL68	BB	Tb427.10.600	Tb927.10.600	Q38CI0	541	62-258, 264-294, 304-341, 346-450	264-294, 304-341 built as UNK
mL70	BD	Tb427.06.4200	Tb927.6.4200	Q586Y7	547	105-521	
mL71	BE	Tb427.07.3460	Tb927.7.3460	Q57WG1	449	11-190, 228-448	
mL72	BF	Tb427.06.3930	Tb927.6.3930	Q585Z1	426	26–62, 118-421	
mL74	BH	Tb427.10.7380	Tb927.10.7380	Q38AM5	349	89-314	
mL75	BI	Tb427.10.380	Tb927.10.380	Q38CK0	342	20-342	
mL76	BJ	Tb427tmp.01.2340	Tb927.11.10570	Q383M2	333	173-333	
mL77	BK	Tb427.06.2480	Tb927.6.2480	Q584Q8	386	84-156, 188-233, 254-269, 280-386	254-259 built as UNK
mL78	BL	Tb427.10.11050	Tb927.10.11050	Q389N4	312	31-130, 141-197, 216-265, 281-306	
mL80	BN	Tb427.06.1440	Tb927.6.1440	Q585A3	302	53-266	
mL81	BO	Tb427tmp.02.3230	Tb927.11.5530	Q385L5	262	36-193, 210-262	

mL83	BQ	Tb427.07.3430	Tb927.7.3430	Q57WF8	231	16-200
mL84	BR	Tb427.06.4080	Tb927.6.4080	Q586A6	205	11-205
mL85	BS	Tb427tmp.160.2250	Tb927.9.3640	Q38FG8	198	20-163

456 **Supplementary File 3. Contacts of assembly factors with rRNA.** Regions and nucleotides of
457 respective rRNA domains are color-coded as in Figure 4. The underscored regions are in mature
458 conformation in the pre-mtLSU.

459

Assembly factor	Contacts with rRNA	
	Region	Nucleotides
mt-EngA	H74, H75, H88, H90-91	868-874, 891-898, 958-967, 994-999, 1004
mt-RbgA	H90-91	1021, 1071
mt-RsfS	H95	1126-1132, 1138-1141
TbLAF2	H39, H43, H72, H74, H88, H93	132-135 347-351, 404, 821-829, 832-835, 860-862, 904, 965-677, 985-992, 1079-1082, 1119
TbLAF3	H43	411-412, 446
TbLAF4	H39, H90-93	351-353, 857-859, 992-994, 1008, 1012-1021, 1071-1087, 1122-1124
TbLAF5	H43, H90, H95	409-413, 1020-1021, 1136-1137
TbLAF6	H13, H28, H37, H80-81, H88	65-66, 164-166, 313, 328, 908, 917-919, 935-939, 944-953
TbLAF7	H41, H43	407, 448-450
TbLAF8	H95	1131-1140
TbLAF9	H80-81, H88	908-909, 915-916, 919-924, 930-940, 952-957, 961
TbLAF10	H26, H32, H33, H35a, H37, H39, H51, H72, H73-75, H80-81, H93	127-139, 199-200, 270-276, 289-293, 306-316, 344-355, 497, 550, 555, 826-828, 847-848, 850-855, 860-862, 870, 903-922, 930-933, 947-980, 955-965, 983 - 992, 1085-1089

460

461 **Materials and Methods**

462 **Strains and growth conditions**

463 *T. brucei* procyclic Lister strain 427 was grown in SDM-80 medium supplemented with 10%
464 fetal bovine serum. Mitochondria were isolated as described earlier [34]. $1.5x10^{11}$ cells were
465 harvested, washed in 20 mM sodium phosphate buffer pH 7.9 with 150 mM NaCl and 20 mM
466 glucose, resuspended in 1 mM Tris-HCl pH 8.0, 1 mM EDTA, and disrupted by 10 stroke in 40
467 ml Dounce homogenizer. The hypotonic lysis was stopped by immediate addition of 1/6 volume
468 of 1.75 M sucrose. Crude mitochondria were pelleted (15 min at 16000 xg, 4°C), resuspended in
469 20 mM Tris-HCl pH 8.0, 250 mM sucrose, 5 mM $MgCl_2$, 0.3 mM CaCl2 and treated with 5
470 µg/ml DNase I for 60 min on ice. DNase I treatment was stopped by addition of one volume of
471 the STE buffer (20 mM Tris-HCl pH 8.0, 250 mM sucrose, 2 mM EDTA) followed by
472 centrifugation (15 min at 16000 xg, 4°C). The pellet was resuspended in 60% Percoll in STE and
473 loaded on the bottom of six 10-35% Percoll gradient in STE in polycarbonate tubes for SW28
474 rotor (Beckman). Gradients were centrifuged for 1 hour at 24000 rpm, 4°C. The middle diffused

475 phase containing mitochondrial vesicles (15-20 ml per tube) was collected, washed twice in the
476 STE buffer, snap-frozen in liquid nitrogen and stored at -80°C.

477 **Purification of mitoribosomes**

478 Mitochondria were further purified further using a stepped sucrose gradient (60 %, 32 %, 23 %,
479 15%) in a low ionic strength buffer (50 mM HEPES/KOH pH 7.5, 5 mM MgOAc, 2 mM
480 EDTA). A thick pellet at the 60-32% interface was collected and lysed by mixing with 5
481 volumes of detergent containing lysis buffer (25 mM HEPES/KOH pH 7.5, 100 mM KCl, 15
482 mM MgOAc, 1.7 % Triton X-100, 2 mM DTT, Complete-EDTA Free Protease Inhibitor). The
483 lysate was centrifuged at 30,000 xg twice, saving the supernatant after each spin. The
484 supernatant was then subjected to differential PEG precipitation; PEG 10,000 was added to reach
485 a concentration of 1.5 % (w/v) and incubated on ice for 10 mins, followed by a spin at 30,000 xg.
486 The supernatant was transferred to a fresh tube, and PEG 10,000 was added to reach a
487 concentration of 8 % (w/v) then incubated on ice for 10 mins, followed by a spin at 30,000 xg.

488 The pellet was then resuspended in 800 µl of lysis buffer and then layered onto a 34% sucrose
489 cushion (25 mM HEPES/KOH pH 7.5, 100 mM KCl, 15 mM MgOAc, 1.0 % Triton X-100, 2
490 mM DTT, Complete-EDTA Free Protease Inhibitor) in a TLA120.2 centrifuge tube (0.4 ml of
491 cushion per tube). Mitoribosomes were pelleted through the cushion by centrifugation at 231,550
492 xg for 45 min. Pelleted mitoribosomes were resuspended using a total of 100 µl of resuspension
493 buffer (25 mM HEPES/KOH pH 7.5, 100 mM KCl, 15 mM MgOAc, 0.01 % β-DDM, 2 mM
494 DTT). The resuspended mitoribosomes were then layered onto a continuous 15-30 % sucrose
495 gradient and centrifuged in a TLS55 rotor for 120 min at 213,626 xg. The gradient was
496 fractionated manually, and fractions containing mitoribosome as judged by the 260 nm
497 absorbance were pooled and buffer exchanged in a centrifugal concentrator.

498 **Cryo-EM and model building**

499 For cryo-EM analysis, 3 µL of the sample at a concentration of OD260 3.5, was applied onto a
500 glow-discharged (20 mA for 30 seconds) holey-carbon grid (Quantifoil R2/2, copper, mesh 300)
501 coated with continuous carbon (of ~3 nm thickness) and incubated for 30 seconds in a controlled
502 environment of 100% humidity and 4 ºC temperature. The grids were blotted for 3 seconds,
503 followed by plunge-freezing in liquid ethane, using a Vitrobot MKIV (FEI/Thermofischer). The
504 data was collected on a FEI Titan Krios (FEI/Thermofischer; Scilifelab, Stockholm, Sweden, and
505 ESRF, Grenoble, Frane) transmission electron microscope operated at 300 keV, using C2
506 aperture of 70 µm; slit width of 20 eV on a GIF quantum energy filter (Gatan). A K2 Summit
507 detector (Gatan) was used to collect images at a pixel size of 1.05 Å (magnification of 130,000X)
508 with a dose of ~35 electrons/Å2 fractionated over 20 frames. A defocus range of 0.8 to 3.5 µm
509 was applied.

510 19,158 Micrographs (after bad images were removed based on real and reciprocal space features)
511 were collected across 5 non-consecutive data acquisition sessions and processed together using
512 RELION. 896,263 particles were picked using Warp and coordinates were imported into
513 RELION for particle extraction at an initial binning factor of two. The particles were subjected to

supervised 3D classification using references generated previously in a screening dataset, which was started based on the Trypanosoma cytosolic ribosome as an initial model.
This crude separation classified the 207,788 particles as mtLSU-like, and the remaining as mature mtLSU-like, SSU-like or monosomes. This subset was subjected to auto-refinement separately to improve the angular assignments and then classified further using fine-angular searches with a solvent mask applied. From the mtLSU-like particles, 32,339 particles were retained as pre-mtLSU of good quality and the rest were discarded as non-particles.
The retained pre-mtLSUs were then subjected to auto-refinement once more to improve the angles further, this time applying a solvent mask during the refinement procedure, and then the 3D reconstructions obtained were used as a reference for CTF refinement to improve the reconstruction. The final map was then estimated for local resolution using RELION and sharpened with a B-factor appropriate for the reconstruction as estimated automatically using the postprocessing procedure.

Model building was done using *Coot* 0.9 [35]. First the model of the mature mtLSU (PDB ID:6HIX) was fitted to the density. Chains present in the pre-mtLSU were then individually fitted and locally refined. Additional chains were modeled de-novo and sequences assigned by direct comparison with the density. All models were refined iteratively using PHENIX [36] realspace refinement and validated using MolProbity [37]. The data collection, model refinement and validation statistics are presented in Supplementary data file1. All figures were prepared either in Chimera [38] or ChimeraX [39] with additional graphical elements created using Inkscape.

Data availability

The electron density map has been deposited in EMDB under accession code EMD-XXX. The model has been deposited in PDB under accession code XXXX. All data is available in the paper or Supplementary Information.

Acknowledgements

The authors thank the SciLifeLab cryo-EM and mass spectrometry facilities. This work was supported by the Swedish Foundation for Strategic Research (FFL15:0325), Ragnar Söderberg Foundation (M44/16), Swedish Research Council (NT_2015-04107), Cancerfonden (2017/1041), European Research Council (ERC-2018-StG-805230), Knut and Alice Wallenberg Foundation (2018.0080), EMBO Young Investigator Program to A.A., and by and by Czech Science Foundation (18-17529S) and ERD fund (CZ.02.1.01/0.0/0.0/16_019/0000759) to A.Z., and by Czech Science Foundation (20-04150Y) to O.G. The cryo-EM facility is funded by the Knut and Alice Wallenberg, Family Erling Persson, and Kempe foundations.

552 **Author contributions**

553 Victor Tobiasson: Formal analysis, Investigation, Validation, Visualization, Writing - original
554 draft, Writing - review and editing

555 Ondřej Gahura: Conceptualization, Data curation, Formal analysis, Investigation, Validation,
556 Visualization, Writing - original draft, Writing - review and editing

557 Shintaro Aibara: Conceptualization, Data curation, Formal analysis, Writing - review and editing

558 Rozbeh Baradaran: Investigation, Validation, Visualization, Writing - review and editing

559 Alena Zíková: Conceptualization, Investigation, Funding acquisition, Project administration,
560 Supervision, Writing - original draft, Writing - review and editing

561 Alexey Amunts: Conceptualization, Investigation, Funding acquisition, Project administration,
562 Resources, Supervision, Validation, Writing - original draft, Writing - review and editing

563

564 **References**

565 1. Ott, M., Amunts, A. & Brown, A. (2016) Organization and Regulation of Mitochondrial
566 Protein Synthesis, *Annu Rev Biochem*.
567 2. Greber, B. J. & Ban, N. (2016) Structure and Function of the Mitochondrial Ribosome, *Annu*
568 *Rev Biochem.* **85**, 103-32.
569 3. Zikova, A., Panigrahi, A. K., Dalley, R. A., Acestor, N., Anupama, A., Ogata, Y., Myler, P. J.
570 & Stuart, K. (2008) Trypanosoma brucei mitochondrial ribosomes: affinity purification and
571 component identification by mass spectrometry, *Mol Cell Proteomics.* **7**, 1286-96.
572 4. Ramrath, D. J. F., Niemann, M., Leibundgut, M., Bieri, P., Prange, C., Horn, E. K., Leitner,
573 A., Boehringer, D., Schneider, A. & Ban, N. (2018) Evolutionary shift toward protein-based
574 architecture in trypanosomal mitochondrial ribosomes, *Science.* **362**.
575 5. Saurer, M., Ramrath, D. J. F., Niemann, M., Calderaro, S., Prange, C., Mattei, S., Scaiola, A.,
576 Leitner, A., Bieri, P., Horn, E. K., Leibundgut, M., Boehringer, D., Schneider, A. & Ban, N.
577 (2019) Mitoribosomal small subunit biogenesis in trypanosomes involves an extensive assembly
578 machinery, *Science.* **365**, 1144-1149.
579 6. Li, N., Chen, Y., Guo, Q., Zhang, Y., Yuan, Y., Ma, C., Deng, H., Lei, J. & Gao, N. (2013)
580 Cryo-EM structures of the late-stage assembly intermediates of the bacterial 50S ribosomal
581 subunit, *Nucleic Acids Res.* **41**, 7073-83.
582 7. Ni, X., Davis, J. H., Jain, N., Razi, A., Benlekbir, S., McArthur, A. G., Rubinstein, J. L.,
583 Britton, R. A., Williamson, J. R. & Ortega, J. (2016) YphC and YsxC GTPases assist the
584 maturation of the central protuberance, GTPase associated region and functional core of the 50S
585 ribosomal subunit, *Nucleic Acids Res.* **44**, 8442-55.
586 8. Jomaa, A., Jain, N., Davis, J. H., Williamson, J. R., Britton, R. A. & Ortega, J. (2014)
587 Functional domains of the 50S subunit mature late in the assembly process, *Nucleic Acids Res.*
588 **42**, 3419-35.
589 9. Davis, J. H., Tan, Y. Z., Carragher, B., Potter, C. S., Lyumkis, D. & Williamson, J. R. (2016)
590 Modular Assembly of the Bacterial Large Ribosomal Subunit, *Cell.* **167**, 1610-1622 e15.
591 10. Nikolay, R., Hilal, T., Qin, B., Mielke, T., Burger, J., Loerke, J., Textoris-Taube, K.,
592 Nierhaus, K. H. & Spahn, C. M. T. (2018) Structural Visualization of the Formation and

593 Activation of the 50S Ribosomal Subunit during In Vitro Reconstitution, *Mol Cell.* **70**, 881-893
594 e3.
595 11. Davis, J. H. & Williamson, J. R. (2017) Structure and dynamics of bacterial ribosome
596 biogenesis, *Philos Trans R Soc Lond B Biol Sci.* **372**.
597 12. Zhang, X., Yan, K., Zhang, Y., Li, N., Ma, C., Li, Z., Zhang, Y., Feng, B., Liu, J., Sun, Y.,
598 Xu, Y., Lei, J. & Gao, N. (2014) Structural insights into the function of a unique tandem GTPase
599 EngA in bacterial ribosome assembly, *Nucleic Acids Res.* **42**, 13430-9.
600 13. Seffouh, A., Jain, N., Jahagirdar, D., Basu, K., Razi, A., Ni, X., Guarne, A., Britton, R. A. &
601 Ortega, J. (2019) Structural consequences of the interaction of RbgA with a 50S ribosomal
602 subunit assembly intermediate, *Nucleic Acids Res.* **47**, 10414-10425.
603 14. Tegunov, D. & Cramer, P. (2019) Real-time cryo-electron microscopy data preprocessing
604 with Warp, *Nat Methods.* **16**, 1146-1152.
605 15. Kimanius, D., Forsberg, B. O., Scheres, S. H. & Lindahl, E. (2016) Accelerated cryo-EM
606 structure determination with parallelisation using GPUs in RELION-2, *Elife.* **5**.
607 16. Achila, D., Gulati, M., Jain, N. & Britton, R. A. (2012) Biochemical characterization of
608 ribosome assembly GTPase RbgA in Bacillus subtilis, *J Biol Chem.* **287**, 8417-23.
609 17. Pausch, P., Steinchen, W., Wieland, M., Klaus, T., Freibert, S. A., Altegoer, F., Wilson, D.
610 N. & Bange, G. (2018) Structural basis for (p)ppGpp-mediated inhibition of the GTPase RbgA, *J*
611 *Biol Chem.* **293**, 19699-19709.
612 18. Barrientos, A., Korr, D., Barwell, K. J., Sjulsen, C., Gajewski, C. D., Manfredi, G.,
613 Ackerman, S. & Tzagoloff, A. (2003) MTG1 codes for a conserved protein required for
614 mitochondrial translation, *Mol Biol Cell.* **14**, 2292-302.
615 19. Gutgsell, N. S., Deutscher, M. P. & Ofengand, J. (2005) The pseudouridine synthase RluD is
616 required for normal ribosome assembly and function in Escherichia coli, *RNA.* **11**, 1141-52.
617 20. Gutgsell, N. S., Del Campo, M., Raychaudhuri, S. & Ofengand, J. (2001) A second function
618 for pseudouridine synthases: A point mutant of RluD unable to form pseudouridines 1911, 1915,
619 and 1917 in Escherichia coli 23S ribosomal RNA restores normal growth to an RluD-minus
620 strain, *RNA.* **7**, 990-8.
621 21. Brown, A., Rathore, S., Kimanius, D., Aibara, S., Bai, X. C., Rorbach, J., Amunts, A. &
622 Ramakrishnan, V. (2017) Structures of the human mitochondrial ribosome in native states of
623 assembly, *Nat Struct Mol Biol*. **24**, 866-9.
624 22. Itoh, Y., Naschberger, A., Mortezaei, N., Herrmann, J. & Amunts, A. (2020) Analysis of
625 translating mitoribosome reveals functional characteristics of protein synthesis in mitochondria
626 of fungi, *bioRxiv* 2020.01.31.929331
627 23. Amunts, A., Brown, A., Bai, X. C., Llacer, J. L., Hussain, T., Emsley, P., Long, F.,
628 Murshudov, G., Scheres, S. H. & Ramakrishnan, V. (2014) Structure of the yeast mitochondrial
629 large ribosomal subunit, *Science.* **343**, 1485-9.
630 24. Amunts, A., Brown, A., Toots, J., Scheres, S. H. W. & Ramakrishnan, V. (2015) Ribosome.
631 The structure of the human mitochondrial ribosome, *Science.* **348**, 95-98.
632 25. Greber, B. J., Bieri, P., Leibundgut, M., Leitner, A., Aebersold, R., Boehringer, D. & Ban, N.
633 (2015) Ribosome. The complete structure of the 55S mammalian mitochondrial ribosome,
634 *Science.* **348**, 303-8.
635 26. Greber, B. J., Boehringer, D., Leibundgut, M., Bieri, P., Leitner, A., Schmitz, N., Aebersold,
636 R. & Ban, N. (2014) The complete structure of the large subunit of the mammalian
637 mitochondrial ribosome, *Nature.* **515**, 283-6.

638 27. Waltz, F., Soufari, H., Bochler, A., Giege, P. & Hashem, Y. (2020) Cryo-EM structure of the
639 RNA-rich plant mitochondrial ribosome, *Nat Plants.* **6**, 377-383.
640 28. Tobiasson, V. & Amunts, A. (2020) Ciliate mitoribosome illuminates evolutionary steps of
641 mitochondrial translation, *Elife.* **9**, e59264.
642 29. Zhu, J., King, M.S., Yu, M., Klipcan, L., Leslie, A.G. and Hirst, J. (2015) Structure of
643 subcomplex Iβ of mammalian respiratory complex I leads to new supernumerary subunit
644 assignments. *Proceedings of the National Academy of Sciences*, **112**, 12087-12092.
645 30. Van Vranken, J.G., Jeong, M.Y., Wei, P., Chen, Y.C., Gygi, S.P., Winge, D.R. and Rutter, J.
646 (2016). The mitochondrial acyl carrier protein (ACP) coordinates mitochondrial fatty acid
647 synthesis with iron sulfur cluster biogenesis. *Elife*, **5**, e17828.
648 31. Masud, A.J., Kastaniotis, A.J., Rahman, M.T., Autio, K.J. and Hiltunen, J.K. (2019).
649 Mitochondrial acyl carrier protein (ACP) at the interface of metabolic state sensing and
650 mitochondrial function. *Biochimica et Biophysica Acta (BBA)-Molecular Cell Research*, **1866**,
651 118540.
652 32. Petrov, A. S., Wood, E. C., Bernier, C. R., Norris, A. M., Brown, A. & Amunts, A. (2019)
653 Structural Patching Fosters Divergence of Mitochondrial Ribosomes, *Mol Biol Evol.* **36**, 207-
654 219.
655 33. Aibara, S., Modelska, A., Singh, V. & Amunts, A. (2020) Structural basis of mitochondrial
656 translation, *Elife.* in press.
657 34. Schneider, A., Charriere, F., Pusnik, M. & Horn, E. K. (2007) Isolation of mitochondria from
658 procyclic Trypanosoma brucei, *Methods Mol Biol.* **372**, 67-80.
659 35. Emsley, P., Lohkamp, B., Scott, W. G. & Cowtan, K. (2010) Features and development of
660 Coot. *Acta Crystallogr. D Biol. Crystallogr*. **66**, 486–501.
661 36. Liebschner, D., Afonine, P.V., Baker, M.L., Bunkóczi, G., Chen, V.B., Croll, T.I., Hintze, B.,
662 Hung, L.W., Jain, S., McCoy, A.J. and Moriarty, N.W. (2019) Macromolecular structure
663 determination using X-rays, neutrons and electrons: recent developments in Phenix. *Acta*
664 *Crystallogr D Struct Biol* **75**, 861–877.
665 37. Williams, JS. et al. (2018) MolProbity: More and better reference data for improved all-atom
666 structure validation. *Protein Science* **27**, 293-315.
667 38. Pettersen, E.F., Goddard, T.D., Huang, C.C., Couch, G.S., Greenblatt, D.M., Meng, E.C. and
668 Ferrin, T.E. (2004) UCSF Chimera – a visualization system for exploratory research and
669 analysis. *Journal of Computational Chemistry* **25**, 1605–1612.
670 39. Goddard, T.D., Huang, C.C., Meng, E.C., Pettersen, E.F., Couch, G.S., Morris, J.H. and
671 Ferrin, T.E. (2018) UCSF ChimeraX: Meeting modern challenges in visualization and analysis.
672 *Protein Science* **27,** 14–25.